THE JOURNAL OF PHYSICAL CHEMISTRY C
A JOURNAL OF THE AMERICAN CHEMICAL SOCIETY

pubs.acs.org/JPCC

Article

Amorphization Toughening Induced by Microcracks in SiO_2 Thin Films

Yuxiang Gao, Yixuan Gao, Yu-Yang Zhang, and Shixuan Du*

Cite This: J. Phys. Chem. C 2023, 127, 8825−8832

Read Online

ACCESS | Metrics & More | Article Recommendations | Supporting Information

ABSTRACT: Fused silica, a widely used facing material of transparent armor, was found to transform into stishovite under heavy shock compression. The ballistic-resistant performance of the partially transformed fused silica, which is highly correlated to the crack initiation and propagation processes, is important for multi-hit possibility. The ultra-high hardness and strength of stishovite are beneficial for the reduction of crack initiation. However, how the pre-existing cracks in stishovite propagate is an open question. Here, by combining molecular dynamics simulations and density functional theory calculations, we investigate the fracture behavior of crystalline stishovite with pre-existing cracks at room temperature. It is found that the crystalline stishovite phase transforms into an amorphous phase via a deformed phase under tensile loading, leading to a ductile fracture. Amorphization is localized on crack tips because of the strain concentration. Amorphization helps to inhibit crack propagation by volume expansion, increasing the final fracture strain. The amorphization mechanism and crack propagation path are robust when the shape of cracks changes. These results provide a reference for application of fused silica-based transparent armor systems.

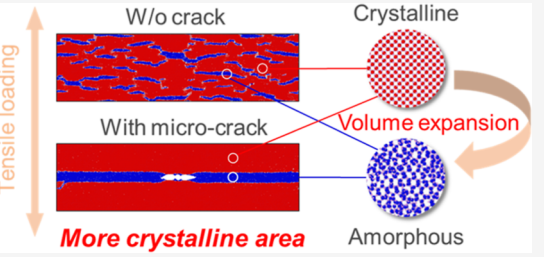

INTRODUCTION

Ceramics are essential in human civilization, with widespread applications in aerospace, automotive engineering, and medical engineering based upon their unique thermal, physical, and mechanical properties.[1−7] Compared with metals and polymers, ceramics possess higher strength, hardness, and better resistance to wear and corrosion.[8−14] But the working situations of ceramics are always limited by their brittleness at room temperature. Reducing the sample size to the nanoscale offers a feasible strategy to design ductile ceramics working at room temperature.[15−20] When the diameter was reduced to 18 nm, unusual strain plasticity of SiO_2 glass nanofibers around room temperature was observed. As the size decreased, the free surface-affected zone increased and more bond-switching events happened per irreversible bond loss, thus introducing plastic deformation in SiO_2 nanofibers.[19,20]

Fused silica has been substantially investigated as a facing material for transparent armor because of its high hardness and transparency.[21−28] Previous studies indicate that fused silica will transform into stishovite when it experiences heavy shock compression, improving the ballistic protection performance.[29−31] The improvement is rooted in the ultra-high hardness of stishovite, which is 5 times harder than the silica glass matrix.[32,33] Despite excellent hardness, brittleness is also an important parameter to evaluate a good transparent armor. It is known that brittleness will lead to the fast propagation of cracks under shock compression and ballistic impact.[34,35] The propagation of cracks will continuously decrease the ballistic resistance under multi-hit impacts. Although the transformation from fused silica to stishovite results in an increase in hardness, which is good for transparent armor, it is still unknown how the pre-existing cracks in stishovite propagate. Therefore, understanding the evolution of the brittleness-induced cracks in stishovite is of great importance for improving the performance of fused silica-based transparent armor.

In this paper, we report the ductile fracture of stishovite single-crystalline thin films with pre-existing cracks at room temperature. In a crack-free lattice, the amorphization appears randomly, resulting in a disordered structure. For thin films with pre-existing cracks, amorphization only appears near crack tips, while most of the ordered structure remains. As cracks exist, the strain concentration at crack tips induces lattice deformation, forming a deformed stishovite phase. Then, the amorphous phase prefers to nucleate near the deformed stishovite phase rather than the pristine stishovite phase. What is more, the fracture behavior of stishovite thin films with pre-existing cracks is size-dependent. The fracture strain increases from 0.12 to 0.44, while the concentration of an amorphous phase increases as the sample width is reduced from 150 to 30

Received: February 21, 2023
Revised: April 14, 2023
Published: May 1, 2023

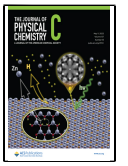

https://doi.org/10.1021/acs.jpcc.3c01189
J. Phys. Chem. C 2023, 127, 8825−8832

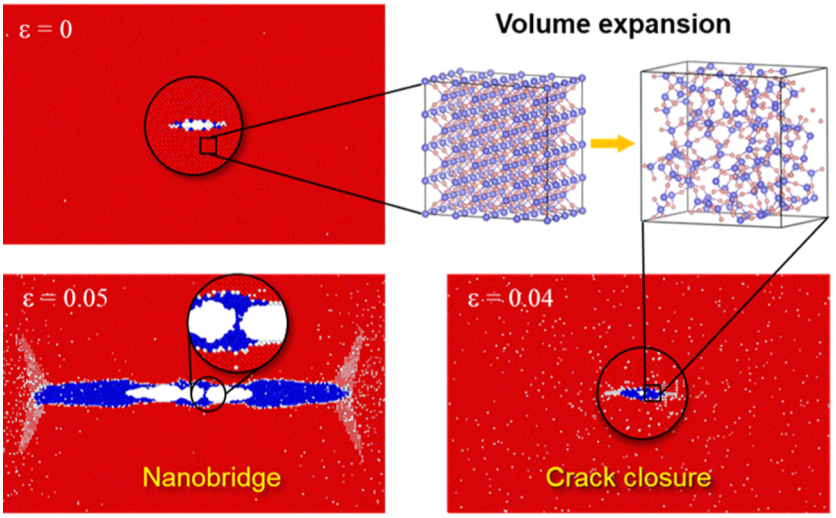

Figure 1. Amorphization toughening mechanism: crack closure induced by volume expansion and nanobridge formation.

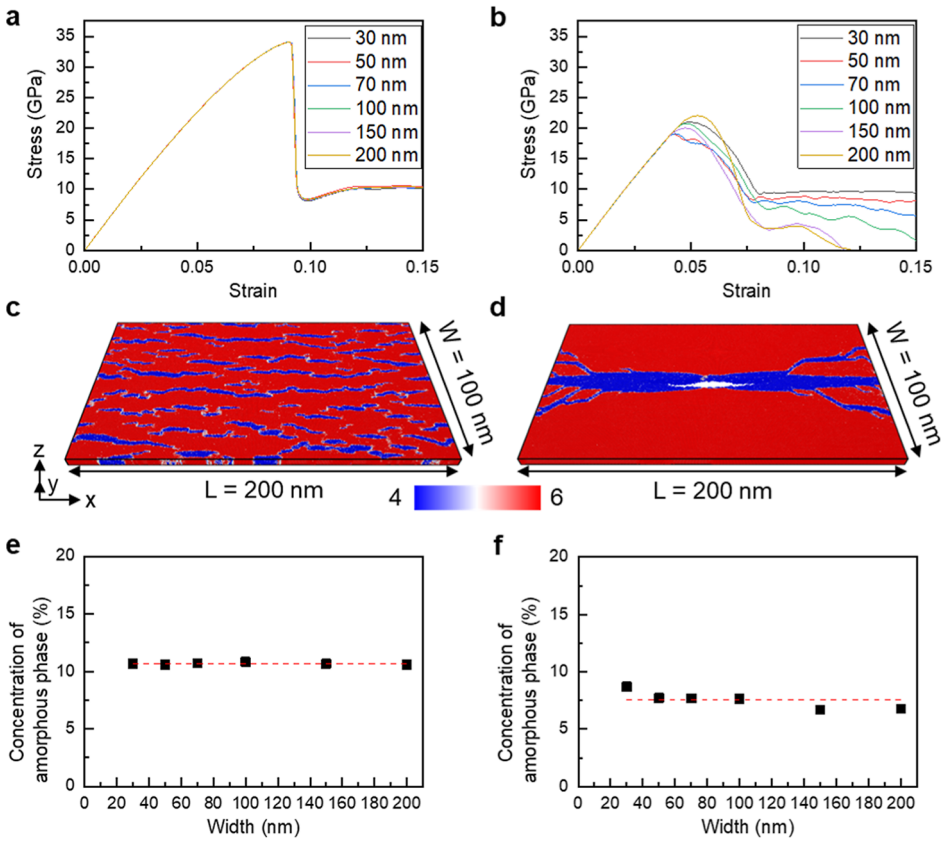

Figure 2. Mechanic property, coordination numbers (CNs), and the concentration of amorphous phases when applying uniaxial tensile stress on stishovite thin films along the *y* direction with and without pre-existing cracks. (a,b) Stress−strain ($\sigma-\varepsilon$) relations of pristine (a) and pre-cracked (b) stishovite thin films with widths of 30, 50, 70, 100, 150, and 200 nm. The crack is 6 nm in length for all thin films. (c,d) 3D views of stishovite thin films without cracks (c) and with pre-existing cracks (d) under 0.1 tensile strain. Si atoms are colored according to the CN, as shown in the bottom color bar. The thickness of stishovite thin films is 5 nm. (e,f) Concentration of an amorphous phase of stishovite thin films under 0.1 tensile strain without crack (e) and with crack (f). The red dashed lines represent the averaged values.

nm. The amorphization toughening mechanism comes from the volume expansion induced by crystalline-to-amorphous transformation and the formation of nanobridges, as shown in Figure 1. We further evaluate the influence of the shape of the pre-existing crack on its propagation. Overall, the shape does not affect the amorphization mechanism and the propagation path, but it affects fracture properties. As the initial crack length increases from 6 nm to 30 nm, the fracture strain decreases at first and then converges at a crack length of 24 nm. The fracture toughness increases at first and converges at a crack length of 12 nm.

https://doi.org/10.1021/acs.jpcc.3c01189
J. Phys. Chem. C 2023, 127, 8825−8832

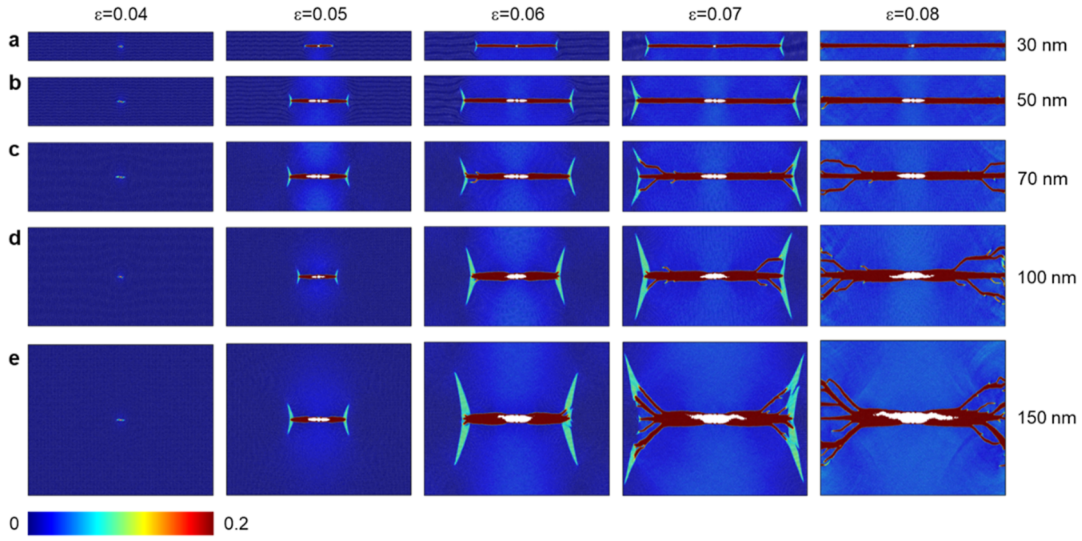

Figure 3. Evolution of the distribution of local shear strains of stishovite thin films in different widths with pre-existing cracks under tensile strains from 0.04 to 0.08. (a) 30 nm, (b) 50 nm, (c) 70 nm, (d) 100 nm, and (e) 150 nm. The initial crack width is 6 nm. The color represents the atomic shear strain, as shown in the bottom color bar. The brown regions indicate the amorphous phase.

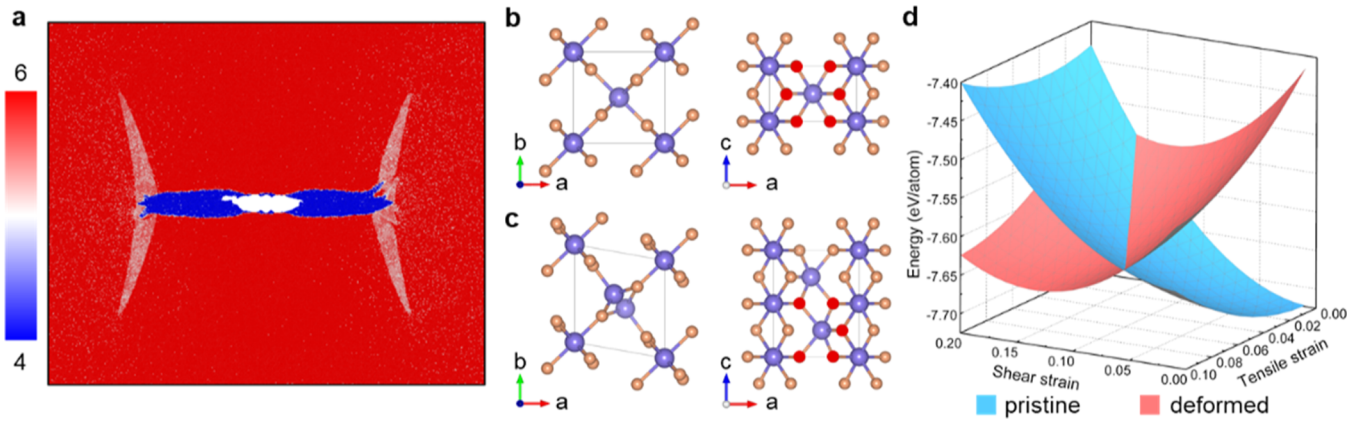

Figure 4. Structure and energy evolution of the deformed phase near crack tips. (a) Si−O coordination distribution of the stishovite film with 150 nm in width under 0.06 tensile strain. The length of the pre-existing crack is 6 nm. Si atoms are colored according to the CN, as shown in the left color bar. (b) Top and side views of the atomic structure of pristine stishovite. (c) Top and side views of the atomic structure of deformed stishovite. In (b,c), the purple and orange pink balls represent Si and O atoms, respectively. The red balls in side views highlight the O atoms bonding to the central Si atom. (d) Strain-dependent energy evolution of pristine and deformed phases.

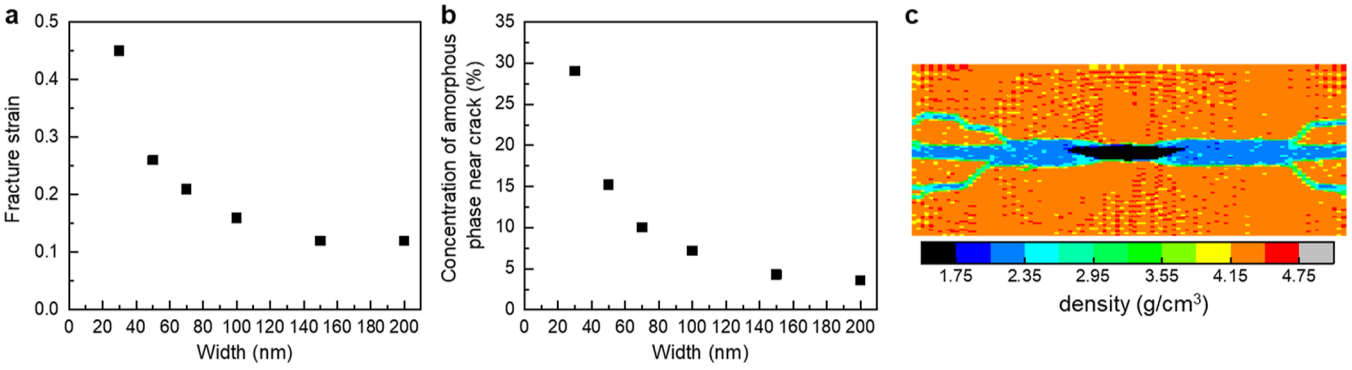

Figure 5. Width-dependent fracture strain and structure of stishovite thin films with a pre-existing crack of 6 nm. (a) Fracture strain. (b) Concentration of the amorphous phase. (c) Mass density map of stishovite thin films with 70 nm in width under a 0.1 tensile strain. The color represents the mass density, as shown in the bottom color bar.

https://doi.org/10.1021/acs.jpcc.3c01189
J. Phys. Chem. C 2023, 127, 8825−8832

THEORETICAL METHODS

Molecular Dynamics Simulation. The interaction between atoms in stishovite was simulated within the framework of a modified Buckingham (BKS) potential[31,36] in the Large-scale Atomic/Molecular Massively Parallel Simulator (LAMMPS).[37] The system temperature was maintained at 300 K by the Nose−Hoover thermostat.[38] The models we used to do the simulation are thin films with 200 nm length, 5 nm thickness, and widths ranging from 30 to 200 nm. A stishovite thin film with a width of 100 nm contains ∼20,000,000 atoms. The cracks in pre-cracked thin films shown in Figures 2, 3, 4, 5 are all 6 nm in length along the x axis. The pre-existing cracks are all perforated along the z axis and generated by removing the corresponding atoms in the center of the stishovite thin film. Periodic boundary conditions were employed along all three directions. A full relaxation was performed for 100 ps before tensile loading was applied. For the tensile test, the strain rate was 10^{-3} ps^{-1}. The loading direction was along the y axis. The time step was set to be 1 femtosecond.

First-Principles Calculation. First-principles calculations based on density functional theory (DFT) were performed by using the Vienna ab initio simulation package (VASP).[39,40] The projector augmented wave (PAW)[41] method was applied with the Perdew−Burke−Ernzerhof (PBE)[42] type exchange−correlation functional. For the potential surface calculations under strains, a kinetic energy cutoff of 750 eV was used. For the pristine stishovite phase, we used a 1 × 1 × 2 supercell, which contains 4 Si atoms and 8 O atoms. For the deformed stishovite phase, a unit cell was used, which is monoclinic and contains 4 Si atoms and 8 O atoms. The k-point sampling was 6 × 6 × 6, generated by Monkhorst−Pack grids with the origin at the Γ-point.[43] The convergence criterion of electronic relaxation was 10^{-6} eV.

To calculate the energies of the pristine stishovite, deformed stishovite, and amorphous phase, a kinetic energy cutoff of 400 eV was used. The atomic models included a 4 × 4 × 4 supercell for the pristine stishovite phase and a 4 × 4 × 2 supercell for the deformed stishovite phase. The atomic model of the amorphous phase was generated by MD simulations, containing 128 Si atoms and 256 O atoms. The structures were relaxed until the residual force on each atom was smaller than 0.05 eV/Å. The k-point sampling was Gamma only for relaxation and 2 × 2 × 2 for self-consistent calculations. The convergence criterion of electronic relaxation was 10^{-5} eV.

RESULTS AND DISCUSSION

Stress−strain curves of pristine and pre-cracked stishovite single crystalline thin films under uniaxial tensile stress applied along the y axis are presented in Figure 2a,b, respectively. These thin films are 200 nm in length and 5 nm in thickness, with widths ranging from 30 to 200 nm. The stress−strain curves of pristine stishovite thin films show that the stress remains the same with increasing sample sizes, while samples with pre-existing cracks apparently present size-dependent behavior. Figure 2a presents that in pristine stishovite, the stress first increases linearly with the increase of strain, with an elastic modulus of 489 GPa, which is consistent with previous work.[44] Then, the stress drops suddenly at 0.09 strain, and the yield stress is around 34 GPa. Figure 2b presents the same increasing tendency of stress with increasing strain at a small strain area. When the strain reaches 0.04, the stress of samples with different widths starts to decrease at different values ranging from 19 to 21 GPa. The drop in the stress usually indicates the occurrence of bond breaking or switching and some defects.

The atomic configuration of the pristine sample with a width of 100 nm under 0.1 tensile strain is shown in Figure 2c. The Si atoms are colored according to the silicon coordination number (CN). Amorphous silica is observed and distinguished by the CN difference. Si atoms in the stishovite phase are octahedrally coordinated by oxygen atoms (CN = 6) and colored in red, while those in the amorphous phase are tetrahedrally coordinated (CN = 4) and colored in blue. Amorphization is found to initiate throughout whole films randomly in a homogeneous nucleation manner.[31] But when cracks exist, the amorphous phase only forms near cracks under 0.1 tensile strain, as shown in Figure 2d. The concentration of silicon atoms in the amorphous phase for samples with and without pre-existing cracks under 0.1 tensile strain is shown in Figure 2f,e, respectively. It is found that for samples with and without pre-existing cracks, averagely 7.54 and 10.67% of the crystalline silica transforms into the amorphous phase, respectively. The crystalline-to-amorphous transformation is nonelastic since most of the amorphous phase fails to return to the crystalline phase even when the stress is fully released, as shown in Figure S1, which is consistent with previous works.[45,46] According to our simulations, localized amorphization renders the advantage of retaining a more intact crystalline area. The intact area could keep the high hardness and strength of the stishovite phase, which may be helpful in reducing the damage caused by multi-hit ballistic impact. The analysis and simulations also indicate that the amorphization mechanisms behind them are highly correlated to the existence of cracks or maybe other defects.

In order to figure out the mechanism of amorphization with pre-existing cracks, we carried out atomic strain analysis for samples with 30, 50, 70, 100, and 150 nm widths. In Figure 3, we show the atomically resolved shear strain maps of the thin films with tensile strains from 0.04 to 0.08 to investigate the development of plastic deformation since the stress−strain curves of all pre-cracked samples drop in this range. The shear strain maps under 0.04 tensile strain show that a large shear strain concentration appears at the crack tip with a value around 0.1. Then, the brown regions initiate from the crack tips and propagate perpendicular to the applied stress orientation until tensile strains reach 0.06. According to the corresponding configurations in Figure S2, the brown regions are amorphous phases with a shear strain of atoms close to 1. Despite the brown regions, we notice that there are cyan regions in a "fishtail-like" shape with a shear strain value of ∼0.1. It should be mentioned that a new phase is found in these regions, which will be discussed in Figure 4. As the tensile strain further increases to 0.07 and 0.08, the amorphous phase branches into two or three paths and grows at an angle of ∼45° to the applied stress. The number of branches increases as the tensile strain increases. For all thin films except the 30 nm one, the branched amorphous phase (Figure S2) only initiates in the strain concentration area (Figure 3). Once the amorphization is completed, the local shear strain is released. All these analyses indicate that the amorphization demands the local strain concentration.

The configuration of the "fishtail-like" regions (Figures 3 and S2) exhibits a previously unknown monoclinic phase of SiO_2. The coordination analysis of the stishovite thin film under 0.06 tensile strain is shown in Figure 4a. As shown in Figure 4a, the

https://doi.org/10.1021/acs.jpcc.3c01189
J. Phys. Chem. C 2023, 127, 8825−8832

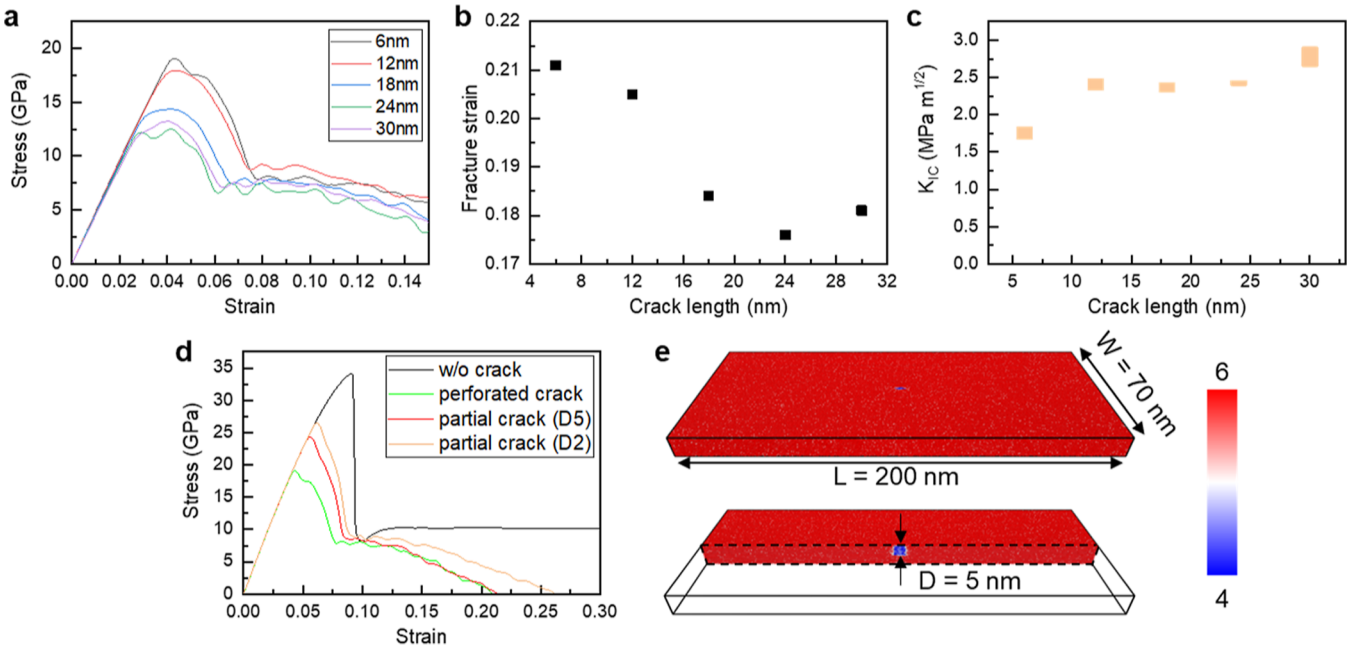

Figure 6. Uniaxial tensile stress applied on stishovite thin films of 70 nm widths with pre-existing cracks of different lengths and penetration depths. (a) Stress−strain ($\sigma-\varepsilon$) relations. (b) Fracture strain. (c) Fracture toughness. The initial lengths of cracks are 6, 12, 18, 24, and 30 nm. (d) Stress−strain ($\sigma-\varepsilon$) relations of stishovite thin films without cracks, with perforated cracks, and with partial cracks. The penetration depths of partial cracks are 2 and 5 nm. (e) 3D atomic configuration of a thin film under a 0.05 strain with a 5 nm deep partial crack. The thickness of thin films is 10 nm. Si atoms are colored according to the Si−O coordination number, as shown in the right color bar.

CN of Si atoms in stishovite is 6, while that in amorphous regions is 4. It is found that the CN of Si atoms in the "fishtail-like" region is between 4 and 6, indicating that it may be an intermediate phase. The atomic structures of pristine stishovite and the intermediate phase are shown in Figure 4b,c, respectively. The main difference between them is the CN of central Si atoms. As highlighted by red balls in Figure 4b,c, the central Si atom is coordinated with six surrounding O atoms in the pristine stishovite phase, while it is coordinated with 5 oxygen atoms in the deformed stishovite phase.

Since the deformed stishovite phase only appears at the local strain concentration region, we carried out first-principles calculations to investigate the effect of strain conditions on the transformation from the pristine to the deformed phase. The potential energy surfaces of the pristine phase (pink) and the deformed phase (sky blue) under strain are shown in Figure 4d. The tensile strain ranges from 0 to 0.1, and the shear strain ranges from 0 to 0.2. Apparently, the pristine phase is more energy favorable when the lattice is fully relaxed. As the strain increases, either tensile strain or shear strain, the energy of the deformed phase decreases rapidly, while the energy of the pristine phase increases. The intersection of the two potential surfaces represents the phase transformation. The phase transformation does not induce volume change. Specifically, under a 0.05 tensile strain, the phase transformation occurs at a 0.11 shear strain. The values of strain are consistent with those obtained from our MD simulation, in which the shear strain is ~0.1 when the fishtail-like region appears at a tensile strain of 0.05−0.06.

To clarify whether the deformed phase plays an important role in the amorphization process, we also compared the energy of the pristine stishovite phase, the deformed stishovite phase, and the amorphous phase. The energy of the amorphous phase is 11.58 kJ/mol higher than that of the pristine stishovite phase. The energy difference provides a good guideline for the energy input required to amorphize materials. DFT calculations agree well with the previous works that the enthalpies of the crystalline to amorphous transition in Si and Ge are 11.6 and 11.9 kJ/mol, respectively.[47] Compared to the pristine stishovite phase, the energy difference between the amorphous phase and the deformed stishovite phase is 4.06 kJ/mol, much lower than that between pristine and amorphous stishovite. The deformation of the stishovite phase contributes 7.52 kJ/mol, which is approximately 65% of the energy input for amorphization, explains why the amorphous phase initiates from the deformed phase rather than the pristine phase.

Besides the growth of an amorphous phase, the crack also propagates as the tensile strain increases. The fracture strains of thin films with different widths ranging from 30 to 200 nm are summarized in Figure 5a. The fracture strain decreases as the sample width increases and then converges when the sample width reaches 150 nm. Meanwhile, the concentration of the amorphous phase also decreases as the sample width increases, as shown in Figure 5b. These two curves are highly correlated, indicating that amorphization plays an important role in crack propagation. Previous works have found that the formation of an amorphous phase can additionally help inhibit crack propagation by forming amorphous nanobridges in the crack's wake.[48] What is more, the mass density of the amorphous phase is much lower than that of the stishovite phase, as shown in Figure 5c. The crystalline-to-amorphous phase transition leads to significant volume expansion,[49,50] inhibiting the expansion of cracks. Thus, the more phase transition occurs, the more volume expands, making the thin film sustain more tensile strains.

Since the crack shape is variable in actual applications, we also test initial cracks with different lengths and perforated depths to evaluate the influence of the crack shape on its

https://doi.org/10.1021/acs.jpcc.3c01189
J. Phys. Chem. C 2023, 127, 8825−8832

propagation. The stress−strain curves of stishovite thin films with pre-existing cracks of 6, 12, 18, 24, and 30 nm lengths are shown in Figure 6a. The stress of samples with cracks in different lengths first increases linearly with increasing strain and then decreases at different strain values ranging from 0.28 to 0.43. The fracture strains of samples with different crack lengths are summarized in Figure 6b. As the initial crack length increases from 6 to 30 nm, the fracture strain decreases at first and then converges at a crack length of 24 nm. The fracture toughness (K_{Ic}) of samples with cracks in different lengths is summarized in Figure 6c. K_{Ic} is calculated according to the following equation

$$K_{Ic} = f\sigma_c\sqrt{\pi c} \quad (1)$$

where $f = \sqrt{\frac{\tan\left(\frac{\pi c}{L}\right)}{\frac{\pi c}{L}}}$ is the geometry factor,[51] c is the half crack length, and σ_c is the critical far-field stress for crack propagation to occur. The results indicate that the fracture toughness first increases as the initial crack length increases and then converges at a crack length of 12 nm. The saturation of fracture toughness of thin films with the increase of the crack length is contributed by crystalline-to-amorphous transformation toughening.[52,53] Figure 6d shows the stress−strain curves of samples with partially perforated pre-existing cracks of 2 and 5 nm penetration depths. The yield stress increases as the penetration depth decreases. The samples with partial perforated cracks are 200 nm in length, 70 nm in width, and 10 nm in thickness, as shown in Figure 6e. The cracks are partially perforated along the z axis.

Despite the variable fracture properties, the amorphization mechanism is robust for different crack shapes. For perforated cracks with different lengths, the amorphous phase initiates at the crack tips and then propagates perpendicular to the applied stress, as shown in Figure S3. The deformed stishovite phase also appears under 0.05 tensile strain. For partially perforated cracks, the amorphization starts at the crack tips, and then the amorphous phase spreads along the z axis under 0.06 tensile strain, as shown in Figure S4. After fully penetrating the stishovite thin films, the amorphous phase propagates perpendicular to the applied stress. The deformed stishovite phase appears at 0.06 tensile strain and 0.07 tensile strain for cracks with 5 and 2 nm penetration depths, respectively. These results indicate that the amorphization process and crack propagation path for samples with an initial crack in different shapes are basically the same.

CONCLUSIONS

Based on MD simulations and DFT calculations, it is found that the pre-existing cracks result in localized amorphization of stishovite thin films. The stishovite phase transforms into the amorphous phase via a deformed stishovite phase induced by a local shear strain concentration. The localized amorphization leads to volume expansion, which inhibits crack propagation. Furthermore, we found that the shapes of the pre-existing crack do not affect the amorphization mechanism and propagation path but do affect fracture properties.

ASSOCIATED CONTENT

Supporting Information

The Supporting Information is available free of charge at https://pubs.acs.org/doi/10.1021/acs.jpcc.3c01189.

Atomic structures of stishovite thin films with pre-existing cracks under strain (PDF)

AUTHOR INFORMATION

Corresponding Author

Shixuan Du − *Chinese Academy of Sciences, Institute of Physics and University of Chinese Academy of Sciences, Beijing 100190, China; Beijing National Center for Condensed Matter Physics, Beijing 100190, China; Songshan Lake Materials Laboratory, Dongguan 523808, China;* orcid.org/0000-0001-9323-1307; Email: sxdu@iphy.ac.cn

Authors

Yuxiang Gao − *Chinese Academy of Sciences, Institute of Physics and University of Chinese Academy of Sciences, Beijing 100190, China;* orcid.org/0000-0002-5574-1792

Yixuan Gao − *Chinese Academy of Sciences, Institute of Physics and University of Chinese Academy of Sciences, Beijing 100190, China;* orcid.org/0000-0003-4694-3955

Yu-Yang Zhang − *Chinese Academy of Sciences, Institute of Physics and University of Chinese Academy of Sciences, Beijing 100190, China;* orcid.org/0000-0002-9548-0021

Complete contact information is available at: https://pubs.acs.org/10.1021/acs.jpcc.3c01189

Author Contributions

The manuscript was written through contributions of all authors. All authors have given approval to the final version of the manuscript. Y.G. performed the simulations and analyzed the results under the guidance of S.D. Y.G. and Y.Z. contributed to the discussion of the project. S.D. conceived the idea of this work and supervised the research.

Notes

The authors declare no competing financial interest.

ACKNOWLEDGMENTS

This work was supported by the National Key Research and Development Program of China (grant no. 2019YFA0308500), the National Natural Science Foundation of China (grant nos. 61888102 and 52201231), the Strategic Priority Research Program of Chinese Academy of Sciences (grant nos. XDB30000000), the CAS Project for Young Scientists in Basic Research (YSBR-003), and the Fundamental Research Funds for the Central Universities.

REFERENCES

(1) Yin, X. W.; Kong, L.; Zhang, L. T.; Cheng, L.; Travitzky, N.; Greil, P. Electromagnetic properties of Si-C-N based ceramics and composites. *Int. Mater. Rev.* **2014**, *59*, 326−355.

(2) Muir, C.; Swaminathan, B.; Fields, K.; Almansour, A. S.; Sevener, K.; Smith, C.; Presby, M.; Kiser, J. D.; Pollock, T. M.; Daly, S. A machine learning framework for damage mechanism identification from acoustic emissions in unidirectional SiC/SiC composites. *npj Comput. Mater.* **2021**, *7*, 146.

(3) Li, W.; Yang, X.; Wang, S.; Xiao, J.; Hou, Q. Research and prospect of ceramics for automotive disc-brakes. *Ceram. Int.* **2021**, *47*, 10442−10463.

(4) Denry, I.; Kelly, J. R. Emerging ceramic-based materials for dentistry. *J. Dent. Res.* **2014**, *93*, 1235−1242.

(5) Zhang, J.; Xu, B.; Xiong, Y.; Ma, S.; Wang, Z.; Wu, Z.; Zhao, S. Design high-entropy carbide ceramics from machine learning. *npj Comput. Mater.* **2022**, *8*, 5.

(6) Ablitt, C.; Craddock, S.; Senn, M. S.; Mostofi, A. A.; Bristowe, N. C. The origin of uniaxial negative thermal expansion in layered perovskites. *npj Comput. Mater.* **2017**, *3*, 44.
(7) Guo, H.; Yang, T.; Xuan, X.; Zhang, Z.; Guo, W. Flexoelectricity in hexagonal boron nitride monolayers. *Extreme Mech. Lett.* **2022**, *52*, 101669.
(8) Chen, W. C.; Schmidt, J. N.; Yan, D.; Vohra, Y. K.; Chen, C. C. Machine learning and evolutionary prediction of superhard B-C-N compounds. *npj Comput. Mater.* **2021**, *7*, 114.
(9) Kaur, G.; Kumar, V.; Baino, F.; Mauro, J. C.; Pickrell, G.; Evans, I.; Bretcanu, O. Mechanical properties of bioactive glasses, ceramics, glass-ceramics and composites: State-of-the-art review and future challenges. *Mater. Sci. Eng., C* **2019**, *104*, 109895.
(10) Xiao, J.; Wen, B.; Xu, B.; Zhang, X.; Wang, Y.; Tian, Y. Intersectional nanotwinned diamond-the hardest polycrystalline diamond by design. *npj Comput. Mater.* **2020**, *6*, 119.
(11) Domnich, V.; Reynaud, S.; Haber, R. A.; Chhowalla, M. Boron Carbide: Structure, Properties, and Stability under Stress. *J. Am. Ceram. Soc.* **2011**, *94*, 3605−3628.
(12) Oliete, P. B.; Peña, J. I.; Larrea, A.; Orera, V.; LLorca, J.; Pastor, J.; Martín, A.; Segurado, J. Ultra-high-strength nanofibrillar Al_2O_3−YAG−YSZ eutectics. *Adv. Mater.* **2007**, *19*, 2313−2318.
(13) Qin, W.; Lei, B.; Peng, C.; Wu, J. Corrosion resistance of ultra-high purity porous alumina ceramic support. *Mater. Lett.* **2015**, *144*, 74−77.
(14) Medvedovski, E. Wear-resistant engineering ceramics. *Wear* **2001**, *249*, 821−828.
(15) Taloni, A.; Vodret, M.; Costantini, G.; Zapperi, S. Size effects on the fracture of microscale and nanoscale materials. *Nat. Rev. Mater.* **2018**, *3*, 211−224.
(16) Nemeth, N. N.; Evans, L. J.; Jadaan, O. M.; Sharpe, W.; Beheim, G.; Trapp, M. Fabrication and probabilistic fracture strength prediction of high-aspect-ratio single crystal silicon carbide micro-specimens with stress concentration. *Thin Solid Films* **2007**, *515*, 3283−3290.
(17) Kang, K.; Cai, W. Size and temperature effects on the fracture mechanisms of silicon nanowires: Molecular dynamics simulations. *Int. J. Plast.* **2010**, *26*, 1387−1401.
(18) Zhang, N.; Asle Zaeem, M. Effects of specimen size and yttria concentration on mechanical properties of single crystalline yttria-stabilized tetragonal zirconia nanopillars. *J. Appl. Phys.* **2017**, *122*, 014302.
(19) Luo, J.; Wang, J.; Bitzek, E.; Huang, J. Y.; Zheng, H.; Tong, L.; Yang, Q.; Li, J.; Mao, S. X. Size-dependent brittle-to-ductile transition in silica glass nanofibers. *Nano Lett.* **2016**, *16*, 105−113.
(20) Bonfanti, S.; Ferrero, E. E.; Sellerio, A. L.; Guerra, R.; Zapperi, S. Damage accumulation in silica glass nanofibers. *Nano Lett.* **2018**, *18*, 4100−4106.
(21) Chakraborty, R.; Dey, A.; Mukhopadhyay, A. K. Loading rate effect on nanohardness of soda-lime-silica glass. *Metall. Mater. Trans. A* **2010**, *41*, 1301−1312.
(22) Salem, J. A. Transparent armor ceramics as spacecraft windows. *J. Am. Ceram. Soc.* **2013**, *96*, 281−289.
(23) Subhash, G. Transparent armor materials. *Exp. Mech.* **2013**, *53*, 1−2.
(24) Kotz, F.; Arnold, K.; Bauer, W.; Schild, D.; Keller, N.; Sachsenheimer, K.; Nargang, T. M.; Richter, C.; Helmer, D.; Rapp, B. E. Three-dimensional printing of transparent fused silica glass. *Nature* **2017**, *544*, 337−339.
(25) Sun, G.; Wang, W.; Bi, J. High-temperature mechanical behavior of boron nitride nanosheets/fused silica composites. *Ceram. Int.* **2020**, *46*, 29330−29333.
(26) Kotz, F.; Risch, P.; Arnold, K.; Sevim, S.; Puigmartí-Luis, J.; Quick, A.; Thiel, M.; Hrynevich, A.; Dalton, P. D.; Helmer, D.; et al. Fabrication of arbitrary three-dimensional suspended hollow microstructures in transparent fused silica glass. *Nat. Commun.* **2019**, *10*, 1439.
(27) Kotz, F.; Quick, A. S.; Risch, P.; Martin, T.; Hoose, T.; Thiel, M.; Helmer, D.; Rapp, B. E. Two-photon polymerization of nanocomposites for the fabrication of transparent fused silica glass microstructures. *Adv. Mater.* **2021**, *33*, 2006341.
(28) Akatsu, T.; Takiguchi, Y.; Shinoda, Y.; Wakai, F.; Muto, H. Optical transmittance and electrical conductivity of silica glass with biserial and hierarchical network structures made of carbon nanofibers. *Ceram. Int.* **2022**, *48*, 36515−36520.
(29) Tracy, S. J.; Turneaure, S. J.; Duffy, T. S. In situ X-Ray diffraction of shock-compressed fused silica. *Phys. Rev. Lett.* **2018**, *120*, 135702.
(30) Grujicic, M.; Snipes, J. S.; Ramaswami, S. The effect of fused-silica pre-shocking on its devitrification propensity and ballistic resistance: an all-atom molecular-level analysis. *J. Mater. Sci.* **2016**, *51*, 3500−3512.
(31) Shen, Y.; Jester, S. B.; Qi, T.; Reed, E. J. Nanosecond homogeneous nucleation and crystal growth in shock-compressed SiO_2. *Nat. Mater.* **2016**, *15*, 60−65.
(32) Léger, J. M.; Haines, J.; Schmidt, M.; Petitet, J. P.; Pereira, A. S.; da Jornada, J. A. H. Discovery of hardest known oxide. *Nature* **1996**, *383*, 401.
(33) Chen, Y.; Hu, X.; Lin, T.; Li, Y.; Ling, Z. Obtaining transparent silica glass from nano-silica hydrosol. *Ceram. Int.* **2021**, *47*, 19340−19345.
(34) Livne, A.; Bouchbinder, E.; Svetlizky, I.; Fineberg, J. The near-tip fields of fast cracks. *Science* **2010**, *327*, 1359−1363.
(35) Rozen-Levy, L.; Kolinski, J. M.; Cohen, G.; Fineberg, J. How fast cracks in brittle solids choose their path. *Phys. Rev. Lett.* **2020**, *125*, 175501.
(36) van Beest, B. W. H.; Kramer, G. J.; van Santen, R. A. Force fields for silicas and aluminophosphates based on ab initio calculations. *Phys. Rev. Lett.* **1990**, *64*, 1955−1958.
(37) Plimpton, S. Fast parallel algorithms for short-range molecular dynamics. *J. Comput. Phys.* **1995**, *117*, 1−19.
(38) Hoover, W. G. Canonical dynamics: Equilibrium phase-space distributions. *Phys. Rev. A* **1985**, *31*, 1695−1697.
(39) Kresse, G.; Furthmüller, J. Efficiency of ab-initio total energy calculations for metals and semiconductors using a plane-wave basis set. *Comput. Mater. Sci.* **1996**, *6*, 15−50.
(40) Kresse, G.; Furthmüller, J. Efficient iterative schemes for ab initio total-energy calculations using a plane-wave basis set. *Phys. Rev. B* **1996**, *54*, 11169−11186.
(41) Blöchl, P. E. Projector augmented-wave method. *Phys. Rev. B* **1994**, *50*, 17953−17979.
(42) Perdew, J. P.; Burke, K.; Ernzerhof, M. Generalized gradient approximation made simple. *Phys. Rev. Lett.* **1996**, *77*, 3865−3868.
(43) Monkhorst, H. J.; Pack, J. D. Special points for Brillouin-zone integrations. *Phys. Rev. B* **1976**, *13*, 5188−5192.
(44) Yang, R.; Wu, Z. Elastic properties of stishovite and the $CaCl_2$-type silica at the mantle temperature and pressure: An ab initio investigation. *Earth Planet. Sci. Lett.* **2014**, *404*, 14−21.
(45) Nishiyama, N.; Wakai, F.; Ohfuji, H.; Tamenori, Y.; Murata, H.; Taniguchi, T.; Matsushita, M.; Takahashi, M.; Kulik, E.; Yoshida, K.; et al. Fracture-induced amorphization of polycrystalline SiO_2 stishovite: a potential platform for toughening in ceramics. *Sci. Rep.* **2014**, *4*, 6558.
(46) Misawa, M.; Ryuo, E.; Yoshida, K.; Kalia, R. K.; Nakano, A.; Nishiyama, N.; Shimojo, F.; Vashishta, P.; Wakai, F. Picosecond amorphization of SiO_2 stishovite under tension. *Sci. Adv.* **2017**, *3*, No. e1602339.
(47) Li, B. Y.; Li, A. C.; Zhao, S.; Meyers, M. A. Amorphization by mechanical deformation. *Mater. Sci. Eng. R Rep.* **2022**, *149*, 100673.
(48) Wang, H.; Chen, D. K.; An, X. H.; Zhang, Y.; Sun, S.; Tian, Y.; Zhang, Z.; Wang, A.; Liu, J.; Song, M.; et al. Deformation-induced crystalline-to-amorphous phase transformation in a CrMnFeCoNi high-entropy alloy. *Sci. Adv.* **2021**, *7*, No. eabe3105.
(49) Zhang, N.; Asle Zaeem, M. Nanoscale self-healing mechanisms in shape memory ceramics. *npj Comput. Mater.* **2019**, *5*, 54.
(50) Mesgarnejad, A.; Karma, A. Vulnerable window of yield strength for swelling-driven fracture of phase-transforming battery materials. *npj Comput. Mater.* **2020**, *6*, 58.

https://doi.org/10.1021/acs.jpcc.3c01189
J. Phys. Chem. C 2023, 127, 8825−8832

(51) Hwu, C. Collinear cracks in anisotropic bodies. *Int. J. Fract.* **1991**, *52*, 239−256.
(52) Yoshida, K.; Wakai, F.; Nishiyama, N.; Sekine, R.; Shinoda, Y.; Akatsu, T.; Nagoshi, T.; Sone, M. Large increase in fracture resistance of stishovite with crack extension less than one micrometer. *Sci. Rep.* **2015**, *5*, 10993.
(53) Yoshida, K.; Nishiyama, N.; Sone, M.; Wakai, F. Strength and toughness of nanocrystalline SiO_2 stishovite toughened by fracture-induced amorphization. *Acta Mater.* **2017**, *124*, 316−324.

https://doi.org/10.1021/acs.jpcc.3c01189
J. Phys. Chem. C 2023, 127, 8825−8832